Gyrokinetic Simulations of Momentum Flux Parasitic to Free-Energy Transfer

T. Stoltzfus-Dueck,[1] W. Hornsby,[2] and S. Grosshauser[3]
[1)] *Princeton Plasma Physics Laboratory, Princeton, NJ 08544*
[2)] *Max-Planck-Institut für Plasmaphysik, Boltzmannstr. 2, D-85748 Garching, Germany*
[3)] *Physics Department, University of Bayreuth, Universitätsstrasse 30 Bayreuth, Germany*[a)]

(Dated: November 22, 2021)

Ion Landau damping interacts with a geometrical correction to the ExB drift to cause a non-diffusive outward flux of co-current toroidal angular momentum. Quantitative evaluation of this momentum flux requires nonlinear simulations to determine f_L, the fraction of fluctuation free energy that passes through ion Landau damping, in fully developed turbulence. Nonlinear gyrokinetic simulations with the GKW code confirm the presence of the systematic symmetry-breaking momentum flux. For simulations with adiabatic electrons, f_L scales inversely with the ion temperature gradient, because only ion curvature drive can supply free energy to the electrostatic potential. Although kinetic electrons should in principle relax this restriction, the ion Landau damping measured in collisionless kinetic-electron simulations remained at low levels comparable with ion curvature drive, except when magnetic shear $\hat{s}$ was strong. A set of simulations scanning the electron pitch-angle scattering rate showed only a weak variation of f_L with the electron collisionality. However, collisional-electron simulations with electron temperature greater than ion temperature unambiguously showed electron-curvature drive of ion Landau damping and a corresponding enhancement of the symmetry-breaking momentum flux.

PACS numbers: 52.25.Dg, 52.25.Fi, 52.25.Xz, 52.30.Gz, 52.35.We, 52.55.Dy, 52.55.Fa
Keywords: toroidal rotation, tokamak, transport, intrinsic rotation, rotation reversal

I. INTRODUCTION

Toroidal rotation is significant for the confinement of tokamak plasmas, since it can stabilize instabilities such as resistive wall modes.[1] In future plasma devices including ITER, it will become much more difficult to directly drive a desired rotation profile with neutral-beam injection.[2] For this reason, it is critical that we understand "intrinsic rotation," meaning the rotation of plasmas that are free of applied torque.

Intrinsic rotation has been extensively studied in experiments over the last several decades.[3–6] In contrast to the relatively robust and consistent co-current intrinsic rotation observed in the edge of diverted tokamaks,[7–9] the intrinsic rotation gradient at mid-radius exhibits varied behavior, even transitioning suddenly between relatively flat and hollow rotation profiles in so-called "rotation reversals."[10–14] Extensive efforts across many devices have exposed a complicated dependence of the mid-radius intrinsic rotation gradient on many factors,[15–19] in particular a strong and non-monotonic dependence on electron collisionality.[14,19–21]

The intriguing experimental results have also sparked a broad theoretical effort.[6,22,23] Since the conservation of toroidal angular momentum precludes a self-generated torque,[24,25] and since observed momentum fluxes are much too strong to result from neoclassical transport,[26–28] most research has focused on the evaluation of non-diffusive turbulent momentum fluxes, using global full-F gyrokinetic simulations,[29–32] delta-f gyrokinetic simulations that incorporate global or profile effects,[33–35] and radially local "fluxtube" gyrokinetic simulations.[36–39] For a non-rotating, radially local gyrokinetic model without $\boldsymbol{E} \times \boldsymbol{B}$ shear, symmetry arguments may be used to show that the momentum flux must vanish in the statistical average.[22,40–42] For this reason, local gyrokinetic efforts have focused on various corrections to the fluxtube model, which can introduce symmetry-breaking physics that can drive a nondiffusive momentum flux and push the rotation gradient away from zero.[6,22,23,39,43,44] One class of symmetry breakers is comprised of geometrical corrections to the fluxtube model's simplified evaluation of the plasma drifts.[38] Of particular interest among these, there is a geometrical correction to the $\boldsymbol{E} \times \boldsymbol{B}$ drift that causes a momentum flux of nearly identical form to the energy transfer term that carries out ion Landau damping.[45,46] This relationship implies that the asymmetry in the energy transfer of ion Landau damping, which preferentially transfers energy from the potential ϕ to the ion parallel flows,[46,47] corresponds to an asymmetry in the radial flux of toroidal angular momentum, namely a tendency for co-current momentum to flow outward. Although the basic physics of this mechanism is most easily understood through an axisymmetric example (Figure 1), the exact same mechanism also acts in nonaxisymmetric fluctuations.[45,46]

While analytical arguments can demonstrate the existence and sign of this momentum flux, the quantitative magnitude of the effect depends on the amount of energy transferred through ion Landau damping. Since

[a)] Electronic mail: tstoltzf@princeton.edu

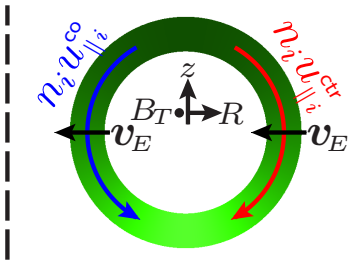

Figure 1. Poloidal cut showing low-frequency axisymmetric fluctuations, with darker green showing positive potential fluctuations, dashed line indicating the symmetry axis, and with major radius R, vertical position z, and toroidal magnetic field B_T. The parallel projection of the (purely poloidal) electric field excites ion parallel flows $n_i u_{\parallel i} \doteq \int \mathrm{d}\mathcal{W}\, f_i v_\parallel$ out of the positive potential, transferring energy from potential ϕ to ion parallel flows. Concurrently, the perpendicular projection of the electric field drives a radial $\boldsymbol{E}\times\boldsymbol{B}$ drift, $\boldsymbol{v}_E$. This drift carries counter-current ion parallel momentum inward and co-current momentum outward, as long as energy is transferred from ϕ to ion parallel flows. For more detailed discussion, including the non-axisymmetric case, see references 45 and 46.

much of this energy transfer is likely to occur in damped modes, a nonlinear numerical study retaining the full turbulent spectrum is needed. In this article, we report the results of such gyrokinetic simulations with the GKW code,[48] verifying the existence of the symmetry-breaking momentum flux in the numerical solutions and exploring the parametric dependence of the ion Landau damping and corresponding momentum flux.

The remainder of the article is organized as follows: Sec. II lays out the necessary theoretical framework for the work. Sec. III presents our numerical results for several different cases: adiabatic electrons in Sec. III A, collisionless kinetic electrons in Sec. III B, and collisional kinetic electrons in Sec. III C. Sec. IV summarizes our main conclusions.

II. FORMULATION

In this section, we present the equations and formulas underlying the results of Sec. III.

We will calculate the parasitic momentum flux in a leading-order, free-energy-conserving delta-f gyrokinetic formulation in fluxtube geometry. We begin with the electrostatic limit[49] of (18) and (21) of Stoltzfus-Dueck and Scott[46] (SDS), neglecting the neoclassical drift term:

$$\begin{aligned}\partial_t f_s =& -\frac{1}{2}\left\{J_0\phi, f_s\right\} - v_\parallel v_{ts}\left[\nabla_\parallel f_s + \frac{Z}{T_s}F_{sM}\nabla_\parallel\left(J_0\phi\right)\right]\\ &+ \left(v_\parallel^2+\mu B\right)\left[\frac{T_s}{Z}\mathcal{K}\left(f_s\right) + F_{sM}\mathcal{K}\left(J_0\phi\right)\right]\\ &+ v_{ts}(\mu\nabla_\parallel B)\partial_{v_\parallel} f_s + \frac{1}{2}\partial_y(J_0\phi)F'_{sM} + C\left(f_s\right), \quad (1)\end{aligned}$$

$$\sum_s Z n_s \int \mathrm{d}\mathcal{W}\, J_0 f_s = \sum_s n_s Z^2 \frac{1-\Gamma_{0s}}{T_s}\phi, \quad (2)$$

in which $\int \mathrm{d}\mathcal{W} = 2\pi B\int_0^\infty \mathrm{d}\mu \int_{-\infty}^\infty \mathrm{d}v_\parallel$. $C(f_s)$, the linearized Landau collision operator described by Peeters et al[48] (PCC), was not explicitly included by SDS.[50] All other notation is the same as SDS, except that all equations in this article are normalized following PCC: The normalized species mass $m_s \doteq m_s^{\mathrm{dim}}/m_{\mathrm{ref}}$, density $n_s \doteq n_s^{\mathrm{dim}}/n_{\mathrm{ref}}$, temperature $T_s \doteq T_s^{\mathrm{dim}}/T_{\mathrm{ref}}$, and thermal speed $v_{ts} \doteq v_{ts}^{\mathrm{dim}}/v_{\mathrm{thref}}$ are defined using a reference mass m_{ref}, density n_{ref}, temperature T_{ref}, and thermal speed $v_{\mathrm{thref}} \doteq (2T_{\mathrm{ref}}/m_{\mathrm{ref}})^{1/2}$. (As PCC, we define dimensional thermal speeds as $v_{ts}^{\mathrm{dim}} \doteq \sqrt{2T_s^{\mathrm{dim}}/m_s^{\mathrm{dim}}}$.[51]) Defining also a reference magnetic field strength B_{ref},[52] major radius R_{ref}, and gyroradius $\rho_{\mathrm{ref}} = m_{\mathrm{ref}}cv_{\mathrm{thref}}/eB_{\mathrm{ref}}$,[53] we have normalized as PCC, except that we normalize perpendicular coordinates x and y to ρ_{ref}.[54,55] The normalized Maxwellian $F_{sM} = \pi^{-3/2}\exp\left(-(v_\parallel^2+2\mu B)\right)$ and its radial gradient

$$F'_{sM} = -\left[\frac{R}{L_{ns}} + (v_\parallel^2 + 2\mu B - \frac{3}{2})\frac{R}{L_{Ts}}\right]F_{sM}, \quad (3)$$

depend spatially only on the parallel coordinate s (due to the s dependence of B). Each species' normalized gradient of density ($R/L_{ns} \doteq R_{\mathrm{ref}}/L_{ns}^{\mathrm{dim}}$) and temperature ($R/L_{Ts} \doteq R_{\mathrm{ref}}/L_{Ts}^{\mathrm{dim}}$) is constant over the whole domain. Although we consider only plasmas in a non-rotating frame, we sometimes must allow a background rotation gradient, in particular for runs to determine plasma viscosity. For such calculations, we add a term $-2F_{sM}v_\parallel b_T R u'/v_{ts}$ to the right-hand side of (3), with the (signed) simple toroidal component of the magnetic direction $b_T = \hat{\boldsymbol{b}}\cdot\hat{\boldsymbol{\varphi}}$ and the (constant) normalized rotation gradient $u' \doteq -(R_{\mathrm{ref}}^2/v_{\mathrm{thref}})\partial_r\Omega$.[56] Ω is the (unnormalized) angular frequency of toroidal rigid rotation, taken positive for rotation in the $+\hat{\boldsymbol{\varphi}}$ direction, which is defined for definiteness to be clockwise when viewed from above. Toroidal magnetic field and plasma current are both in the $+\hat{\boldsymbol{\varphi}}$ direction for all simulations in this article, thus $u' > 0$ indicates rotation that is more co-current in the core than the edge.

Equations (1) and (2) are equivalent to (61) and (73) of PCC in the nonrotating, electrostatic limit, neglecting the neoclassical term and the β' correction to the drifts.[57]

As shown by SDS, equations (1) and (2) nonlinearly conserve the free energy $U_{\delta E} + \sum_s U_{\delta s}$ for $U_{\delta E} \doteq \frac{1}{2}V_{\mathrm{pl}}^{-1}\int \mathrm{d}\mathcal{V}\sum_s n_s Z^2\phi(1-\Gamma_{0s})\phi/T_s$, $U_{\delta s} \doteq V_{\mathrm{pl}}^{-1}\int \mathrm{d}\Lambda\, n_s T_s f_s^2/2F_{sM}$, and $\int \mathrm{d}\Lambda \doteq \int \mathrm{d}\mathcal{V}\int \mathrm{d}\mathcal{W}$, with $\int \mathrm{d}\mathcal{V}$ a spatial integral over the simulation domain and $V_{\mathrm{pl}} \doteq \int \mathrm{d}\mathcal{V}\, 1$ the normalized domain volume. The free-

energy terms $U_{\delta s}$ and U_{δ_E} evolve according to

$$\partial_t U_{\delta s} = \frac{n_s}{V_{\rm pl}} \int \mathrm{d}\Lambda\, f_s \Big[-Z v_{ts} v_\parallel \nabla_\parallel (J_0\phi) + T_s(v_\parallel^2 + \mu B)\mathcal{K}(J_0\phi) + T_s C(f_s)/F_{s_M} \Big] + n_s T_s \Big[\Big(\frac{R}{L_{ns}} - \frac{3}{2}\frac{R}{L_{Ts}}\Big)\Gamma_s + \frac{R}{L_{Ts}} Q_s \Big] \quad (4)$$

$$\partial_t U_{\delta_E} = \sum_s \frac{n_s}{V_{\rm pl}} \int \mathrm{d}\Lambda \Big[Z v_{ts} f_s v_\parallel \nabla_\parallel (J_0\phi) - T_s(v_\parallel^2 + \mu B) f_s \mathcal{K}(J_0\phi) + Z(J_0\phi) C(f_s) \Big] \quad (5)$$

in which we defined the normalized particle and heat fluxes:

$$\Gamma_s \doteq -\frac{1}{V_{\rm pl}} \int \mathrm{d}\Lambda\, \frac{1}{2} f_s \partial_y (J_0\phi), \quad (6)$$

$$Q_s \doteq -\frac{1}{V_{\rm pl}} \int \mathrm{d}\Lambda\, (v_\parallel^2 + 2\mu B) \frac{1}{2} f_s \partial_y (J_0\phi). \quad (7)$$

For viscous runs ($u' \neq 0$), the RHS of (4) has an additional term $2 n_s m_s v_{ts} u' \Pi^{(1)}_{\varphi s}$, with

$$\Pi^{(1)}_{\varphi s} \doteq -\frac{1}{V_{\rm pl}} \int \mathrm{d}\Lambda\, v_\parallel b_T R \frac{1}{2} f_s \partial_y (J_0\phi). \quad (8)$$

For the simulations in this article, positive $\Pi^{(1)}_{\varphi s}$ indicates a radial outflux of co-current momentum. Note that the fluxes Γ_s, Q_s, and $\Pi^{(1)}_{\varphi s}$ have species-dependent normalizations, specifically to $\rho_*^2 n_s^{\rm dim} v_{\rm thref}$ times 1, $T_s^{\rm dim}$, and $(m_s^{\rm dim} v_{ts}^{\rm dim} R_{\rm ref})$, respectively, where $\rho_* \doteq \rho_{\rm ref}/R_{\rm ref}$. Note also that our GKW simulations include additional dissipation that is not explicitly shown in (4) and (5).[58]

For the simulations in Sec. III A, we will use the adiabatic-electron approximation. Instead of simulating the electron distribution function f_e, we will simply replace the electron contributions to (2) with the single term $+(n_e/T_e)(\phi - \langle\phi\rangle)$ on the RHS, with $\langle\cdots\rangle$ indicating the flux-surface average. In this approximation, equations (4) and (5) continue to hold, but the species sum goes only over ions, and the electron term in U_{δ_E} is replaced by $(n_e/2T_e V_{\rm pl}) \int \mathrm{d}\mathcal{V}\, (\phi - \langle\phi\rangle)^2$.

The (normalized) parasitic momentum flux [SDS (36), equivalent to (35) of Ref. 38] is

$$\Pi^{(2)}_\varphi = \sum_s n_s m_s v_{ts} \Pi^{(2)}_{\varphi s}, \quad (9)$$

for

$$\Pi^{(2)}_{\varphi s} \doteq -\rho_* \frac{1}{b_p} \frac{1}{V_{\rm pl}} \int \mathrm{d}\Lambda\, v_\parallel b_T^2 R^2 \frac{1}{2} f_s \nabla_\parallel (J_0\phi). \quad (10)$$

The signed constant b_p is a representative value for the poloidal component of $\hat{\boldsymbol{b}}$, approximately equal to (ϵ/q) for the circular geometry used in this article.[59] Although $\Pi^{(2)}_{\varphi s}$ is normalized like $\Pi^{(1)}_{\varphi s}$, the species-summed momentum fluxes $\Pi^{(1)}_\varphi = \sum_s n_s m_s v_{ts} \Pi^{(1)}_{\varphi s}$, $\Pi^{(2)}_\varphi$, and $\Pi_\varphi \doteq \Pi^{(1)}_\varphi + \Pi^{(2)}_\varphi$ must use a species-independent normalization, $\rho_*^2 n_{\rm ref} m_{\rm ref} v_{\rm thref}^2 R_{\rm ref}$. Note that for up-down symmetric magnetic geometry (always the case for the runs in this article), equations (1) and (2) are invariant under the symmetry transform of Ref. 22, implying that $\Pi^{(1)}_\varphi$ vanishes in the statistical average when $u' = 0$.

For emphasis: equation (1) does not contain the higher-order portion of the $\boldsymbol{E} \times \boldsymbol{B}$ drift that gives rise to $\Pi^{(2)}_\varphi$, or any other higher-order symmetry-breaking terms. However, the dominant contribution of $\Pi^{(2)}_\varphi$ comes from the leading-order portions of f_s and ϕ, so we will estimate $\Pi^{(2)}_\varphi$ simply by evaluating (9) using the numerical solutions to the leading-order problem, equations (1) and (2).

Define next the normalized ion Landau damping free-energy transfer rate,[60]

$$T^\parallel_{\phi i} \doteq -Z n_i v_{ti} \frac{1}{V_{\rm pl}} \int \mathrm{d}\Lambda\, f_i v_\parallel \nabla_\parallel (J_0\phi), \quad (11)$$

and the corresponding ion Landau damping fraction

$$f_L \doteq T^\parallel_{\phi i} / \sum_s n_s T_s \Big[\Big(\frac{R}{L_{ns}} - \frac{3}{2}\frac{R}{L_{Ts}}\Big)\Gamma_s + \frac{R}{L_{Ts}} Q_s \Big], \quad (12)$$

which is just the portion of the total turbulent free energy that passes through ion Landau damping. If we take $b_T^2 R^2 \sim 1$,[61] neglect impurities, and use $m_e \ll m_i$, then we have

$$\Pi^{(2)}_\varphi \approx n_i m_i v_{ti} \Pi^{(2)}_{\varphi i} \sim \frac{1}{2} \frac{m_i}{Z b_p} \rho_* T^\parallel_{\phi i} = \frac{1}{2} \frac{m_i}{Z b_p} \rho_* f_L \sum_s n_s T_s \Big[\Big(\frac{R}{L_{ns}} - \frac{3}{2}\frac{R}{L_{Ts}}\Big)\Gamma_s + \frac{R}{L_{Ts}} Q_s \Big], \quad (13)$$

the normalized version of SDS (38).

In a steady-state rotation profile, the velocity gradient is determined by the balance between viscous and nondiffusive momentum fluxes. In order to estimate the intrinsic rotation gradient, we will typically use two runs: one with $u' = 0$, in which we will calculate the symmetry-breaking flux $\Pi^{(2)}_\varphi$, and a second one with $u' \neq 0$, in which we will calculate only the viscous response $\Pi^{(1)}_\varphi$. Using the latter run, we can estimate the Prandtl number $\mathrm{Pr} \doteq \chi_\varphi/\chi_i$ (again with no impurities) as

$$\mathrm{Pr} = \frac{v_{ti}}{u'} \frac{R}{L_{T_i}} \frac{\Pi^{(1)}_{\varphi i}}{Q_i}. \quad (14)$$

With this in hand, we can estimate the rotation peaking from momentum balance ($\Pi^{(1)}_{\varphi i} + \Pi^{(2)}_{\varphi i} = 0$ for $\Pi^{(1)}_{\varphi i}$ evaluated at the intrinsic-rotation u') to be

$$u' = -\frac{v_{ti}}{\mathrm{Pr}} \frac{R}{L_{T_i}} \frac{\Pi^{(2)}_{\varphi i}}{Q_i}. \quad (15)$$

With this, equation (13) leads to the estimated rotation gradient (assuming $\Gamma_s \ll Q_s$)

$$u' \sim -\frac{1}{2}\frac{\rho_*}{Zb_p}\frac{f_L}{\mathrm{Pr}}\frac{R}{L_{T_i}}\sum_s \frac{n_s}{n_i}T_s\frac{Q_s}{Q_i}\frac{R}{L_{Ts}}. \qquad (16)$$

For runs with $R/L_{T_i} \to 0$, both Q_i and $\Pi^{(1)}_{\varphi i}(u' \neq 0)$ generally remain finite, so $\mathrm{Pr} \to 0$ and (15) and (16) become indeterminate. For these cases, we will take the viscosity to be proportional to the ion heat flux, obtaining the alternate formula

$$u'|_{\mathrm{int}} = -\frac{(\Pi^{(2)}_{\varphi i}/Q_i)|_{\mathrm{int}}}{(\Pi^{(1)}_{\varphi i}/Q_i)|_{\mathrm{visc}}}u'|_{\mathrm{visc}}, \qquad (17)$$

in which both the intrinsic $u' = 0$ run [for $(\Pi^{(2)}_{\varphi i}/Q_i)|_{\mathrm{int}}$] and the paired $u' = u'|_{\mathrm{visc}} \neq 0$ run [for $(\Pi^{(1)}_{\varphi i}/Q_i)|_{\mathrm{visc}}$] are done at otherwise matched parameters, in particular both at $R/L_{T_i} = 0$.

III. NUMERICAL RESULTS

While the analysis of SDS demonstrated the existence, sign, and basic qualitative properties of the parasitic momentum flux $\Pi^{(2)}_{\varphi i}$, nonlinear numerical simulation is required in order to pin down quantitative values and the detailed parametric dependence of the Landau-damping fraction f_L and the resulting momentum flux $\Pi^{(2)}_{\varphi i}$. In this section, we present results from numerical solutions of (1) and (2), considering three different cases: collisionless with adiabatic electrons (Sec. III A), collisionless kinetic electrons (Sec. III B), and collisional kinetic electrons (Sec. III C). The resulting values for f_L and $\Pi^{(2)}_{\varphi}$ may then be used in (13)–(17) to estimate the normalized parasitic momentum flux and resulting rotation gradient, or in SDS (38), (40), and (41) to estimate the dimensional momentum flux and rotation gradient.

All simulations have been done with the GKW code[48] in circular geometry. Calculations of the intrinsic momentum flux $\Pi^{(2)}_{\varphi i}$ are always nonlinear, but the viscous runs (with nonzero background rotation shear, to calculate Pr or $\Pi^{(1)}_{\varphi i}$) are typically quasilinear, at normalized binormal wavenumber $k_y \approx 0.49$.[62,63] We retain only electrons and one species of singly-ionized ions (no impurities), with electron and ion densities and density gradients always set to be equal ($n_e = n_i$, $R/L_{ne} = R/L_{ni} \doteq R/L_n$). Our default parameters are $R/L_{T_i} = 6.9$, $R/L_n = 2.2$, $R/L_{T_e} = 6.9$, $\epsilon \doteq r/R_{\mathrm{ref}} = 0.18$, magnetic shear $\hat{s} = 0.8$, safety factor $q = 1.4$, $T_e = T_i$, and collisionless ions. Our standard (normalized) perpendicular domain size is 78 in the radial direction (x) by 93.6 in the binormal direction (y), with normalized gyroradius $\rho_* = 0.01$ and with 22 toroidal modes. Ions are always used for the "reference" values, so that the normalized ion parameters are all unity, $m_i = n_i = T_i = v_{ti} = 1$. We use the real deuterium mass ratio, $m_e = 2.77 \cdot 10^{-4}$.

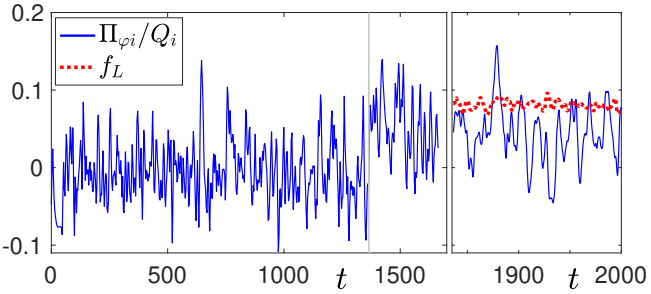

Figure 2. Time trace of $\Pi_{\varphi i}/Q_i$ (blue line) at default parameters with adiabatic electrons. The symmetry-breaking contribution $\Pi^{(2)}_{\varphi i}$ was excluded from the measurement until $t \approx 1365$ (light grey vertical line), after which point $\Pi_{\varphi i}$ shifts to positive values corresponding to a modestly hollow rotation profile. The zoomed-in time trace on the right also shows the ion-Landau-damping fraction f_L (red dots).

A. Adiabatic-electron runs

For the first tests, we simulated the adiabatic-electron limit of (1) and (2), as described in Sec. II. In this limit, the electron heat and particle fluxes vanish identically ($Q_e = \Gamma_e = 0$), so the free-energy source term in (4), which also appears in (12), (13), and (16), contains only ion fluxes.

We consider first a run at the default parameters, which correspond to a strongly-driven ITG regime. Fig. 2 shows the ratio of total ion momentum flux $\Pi_{\varphi i} \doteq \Pi^{(1)}_{\varphi i} + \Pi^{(2)}_{\varphi i}$ to ion heat flux Q_i, as a function of time. The parasitic contribution $\Pi^{(2)}_{\varphi i}$ is excluded from the flux diagnostic at the start of the run, then included starting at (normalized) time $t \approx 1365$.[64] After an initial transient but before $\Pi^{(2)}_{\varphi i}$ is included, the ion momentum flux $\Pi_{\varphi i}$ is instantaneously nonzero but approximately vanishes in the time average, as required by symmetry.[65] After $t \approx 1365$, $\Pi_{\varphi i}$ shifts clearly towards positive values, due to the symmetry-breaking contribution of $\Pi^{(2)}_{\varphi i}$. The late-time average of $\Pi_{\varphi i}/Q_i$ is $+0.044$, roughly consistent with ion Landau damping fraction f_L measured at the same time, also shown in Fig. 2. A matched quasilinear calculation gives $\mathrm{Pr} \approx 0.66$, thus at these parameters equation (15) estimates a hollow rotation profile with $u' \approx -0.45$.

Ion Landau damping can only occur at frequencies near to or lower than the ion transit frequency, so one expects that ion Landau damping and the corresponding $\Pi^{(2)}_{\varphi i}$ would typically be stronger at lower normalized binormal wavenumber k_y. Indeed, the intrinsic momentum flux per toroidal mode number, plotted for default parameters in Fig. 3, shows the expected strong concentration of $\Pi_{\varphi i}$ to lower k_y. Also, unlike $\Pi^{(1)}_{\varphi i}$, which vanishes for axisymmetric ϕ, the parasitic momentum flux $\Pi^{(2)}_{\varphi i}$ takes nonnegligible values even for the axisymmetric modes $k_y = 0$. This is a necessary consequence of ion

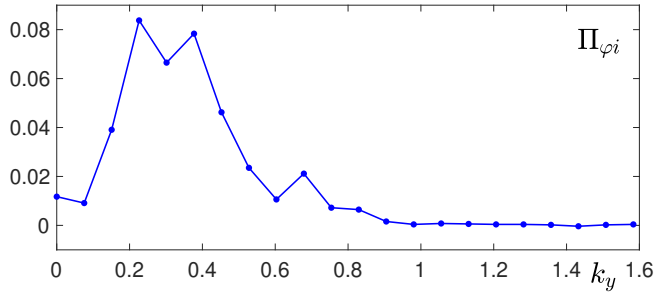

Figure 3. Momentum flux $\Pi_{\varphi i}$ per binormal mode for default parameters, showing much stronger momentum flux at low k_y, including a nonzero contribution from axisymmetric fluctuations ($k_y = 0$).

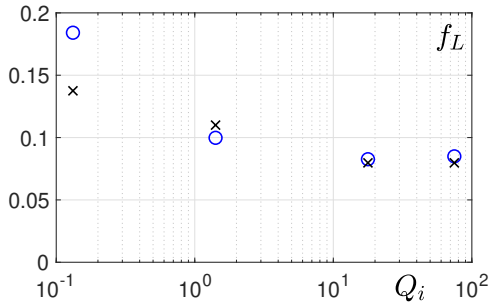

Figure 4. f_L (blue circles) as a function of Q_i for a scan around default parameters (see main text), showing a decreasing f_L (despite increasing u') for more strongly driven ITG turbulence. Much of the variation can be explained be weakened energy transfer into the potential at steeper gradients, as seen from the black x's indicating $f_L^{\rm ad}$ for an assumed-fixed $c_{\mathcal{K}i} = 0.55$.

Landau damping of turbulence-driven zonal flows, as discussed physically in Ref. 45. Nevertheless, the dominant contribution comes from $k_y \neq 0$ modes, where most of the free energy resides.

We also explored parameter dependence, running cases with modified parameters. As shown in Fig. 4, the Landau damping fraction is a decreasing function of driving gradient, taking the largest value $f_L \approx 0.185$ for a marginal case (leftmost point, $R/L_{T_i} = 4.0$, $R/L_n = 1.5$), then dropping for more strongly driven turbulence (moving rightward: $R/L_{T_i} = 5.0$, $R/L_n = 1.5$; default; and $T_e/T_i = 2$). However, equation (16) estimates modestly increasing $|u'|$ for these four cases (L to R: $u' \sim$ -0.10, -0.12, -0.23, and -0.25), due to increasing $(R/L_{T_i})^2$ and decreasing Prandtl numbers (left to right: 1.121, 0.782, 0.66, and 0.62).

What is causing the inverse dependence of f_L on R/L_{T_i}? This question can be at least partially answered by considering the adiabatic-electron limit of the free-energy balance in (4) and (5). The ion Landau damping $T^{\parallel}_{\phi i}$ results from an energy transfer from the $\boldsymbol{E}\times\boldsymbol{B}$ energy ($U_{\delta E}$) into the ion thermal energy ($U_{\delta i}$). However, before such a transfer can occur, the free energy must have somehow moved from $U_{\delta i}$ (which has the only source terms, $\propto Q_s, \Gamma_s$) to $U_{\delta E}$. Equation (5)'s only remaining collisionless term is the curvature transfer $T^{\mathcal{K}}_{\phi i}$ for

$$T^{\mathcal{K}}_{\phi s} \doteq -n_s T_s \frac{1}{V_{\rm pl}} \int {\rm d}\Lambda\, f_s (v_\parallel^2 + \mu B) \mathcal{K}\left(J_0 \phi\right), \qquad (18)$$

which in a collisionless, adiabatic-electron steady state ($\partial_t U_{\delta E} = 0$) must therefore be equal to $T^{\parallel}_{\phi i}$. Setting $T^{\parallel}_{\phi i} = T^{\mathcal{K}}_{\phi i}$, neglecting Γ_i, and using (7), we may then conclude that

$$f_L \approx f_L^{\rm ad} \doteq \frac{c_{\mathcal{K}i}}{R/L_{T_i}}, \text{ for} \qquad (19)$$

$$c_{\mathcal{K}s} \doteq \frac{\int {\rm d}\Lambda\, (v_\parallel^2 + \mu B) f_s \mathcal{K}\left(J_0\phi\right)}{\int {\rm d}\Lambda\, (v_\parallel^2/2 + \mu B) f_s \partial_y (J_0 \phi)}. \qquad (20)$$

The curvature operator has the form $\mathcal{K} \doteq \mathcal{K}^x(s)\partial_x + \mathcal{K}^y(s)\partial_y$, where $\mathcal{K}^y$ is positive at the outboard midplane ($s = 0$) and negative at the inboard midplane ($s = \pm 1/2$), and $\mathcal{K}^x = 0$ at the midplane.[46] If we make a simple small-ϵ, strongly outboard-ballooning estimate $\mathcal{K} \to \partial_y$ and approximate velocities with the thermal speeds ($v_\parallel^2 \sim 1$ and $\mu B \sim 1$), we may crudely estimate $c_{\mathcal{K}i} \sim 4/3$. Since the actual heat flux Q_i will have a finite extent in s, the actual $c_{\mathcal{K}i}$ will typically be somewhat smaller than 4/3, as the integrals in (20) include poloidal positions s with decreasing or even negative $\mathcal{K}^y$. In Fig. 4, black x's show $f_L^{\rm ad}$ inferred with an assumed-constant $c_{\mathcal{K}i} = 0.55$, capturing the qualitative behavior of the plot although not the especially high f_L for the marginal run at $R/L_{T_i} = 4$.

B. Collisionless, kinetic-electron runs

Both the simulation (Fig. 4) and analysis [(19)] in Sec. III A suggest that f_L is fairly constrained in the adiabatic-electron limit, scaling as $(R/L_{T_i})^{-1}$ due to steady-state balance in the adiabatic-electron version of (5). The inclusion of kinetic electrons may allow a richer, more flexible energy balance, as free-energy transfer from electrons can now supply $U_{\delta E}$ with the energy needed to drive ion Landau damping. In this section, we explore this by solving (1) and (2) with kinetic electrons, but still in a (nearly) collisionless limit,[66] conducting a scan of Q_e/Q_i via varying gradients and a scan of the magnetic shear $\hat{s}$, which strongly affects the ion Landau damping channel.

The rotation gradient u' predicted by (16) grows with Q_e/Q_i at fixed f_L, simply because electrons can help ions drive the fluctuating electric fields that cause ion Landau damping, but the viscosity is typically roughly proportional to the ion (not total) heat flux. However, f_L may well also depend on Q_e/Q_i, changing the expected rotation dependence. To examine this, we conducted a series of runs with varying gradients, listed in Table I.

$\frac{R}{L_{T_i}}$	$\frac{R}{L_{T_e}}$	$\frac{R}{L_n}$	Q_i	Q_e	$\Pi_{\varphi i}$	Γ_e	f_L	Pr	$\frac{Q_e}{Q_i}$
6.9	6.9	2.2	62.7	17.7	0.396	1.0	.0550	0.934	0.283
6.9	9	2.2	66.2	26.0	1.45	-1.0	.0462	0.984	0.393
6.9	12	2.2	56.3	33.2	1.53	-2.45	.0362	1.065	0.589
6.9	14.0	2.2	70.7	51.0	1.0	-3.0	.032	1.305	0.721
6.0	15.5	2.2	24.0	24.0	0.64	-1.0	.027	1.206	1.0
6.0	10.5	5.0	43	58	1.55		.0478		1.35
6.0	15.5	5.0	29	61.5	0.95		.0261		2.12
3	9	0	0.274	1.97	.0067	0.7	.0091		7.19
0	9	3	0.837	7.56	.0463	0.177	.0160	(.525)	9.02
0	6	3	.0765	0.777	.0013	0.055	.0066		10.2
0	5	1.5	.0126	0.145	.0001	.0077	.0048	(1.33)	11.5

Table I. Parameters and results for runs plotted in Fig. 5. For cases with $R/L_{T_i} = 0$, Pr is not defined, so $(\Pi^{(1)}_{\varphi i}/u'Q_i)$ from the viscous run is given instead, in parentheses.

In these runs, f_L depends inversely on Q_e/Q_i, as shown in Fig. 5. In fact, if we assume that *no* free energy passes from the electrons through ion Landau damping, so that $T^{\parallel}_{\phi i} = T^{\mathcal{K}}_{\phi i} = c_{\mathcal{K}i} n_i T_i Q_i$ as before, then we may estimate $f_L \approx f_L^{\mathcal{K}i}$ for

$$f_L^{\mathcal{K}s} \doteq \frac{c_{\mathcal{K}s} n_s T_s Q_s}{\sum_{s'} n_{s'} T_{s'} [(R/L_{ns'} - \frac{3}{2} R/L_{Ts'}) \Gamma_{s'} + Q_{s'} R/L_{Ts'}]}. \quad (21)$$

The estimate $f_L \approx f_L^{\mathcal{K}i}$ with $c_{\mathcal{K}i} = 0.5$ and neglecting particle flux Γ_s is also plotted in Fig. 5. It roughly agrees with f_L at most points.

Unlike the adiabatic-electron case [(19)], the scaling $f_L \approx f_L^{\mathcal{K}i}$ is nontrivial and somewhat surprising. Any potential fluctuations ($U_{\delta E}$), whether driven originally by ions or electrons, are able to excite the ion parallel flows that lead to ion Landau damping, at least in principle. Many runs plotted in Fig. 5 had $Q_e \gg Q_i$. Since electrons also drive the potential via curvature transfer $T^{\mathcal{K}}_{\phi e} = c_{\mathcal{K}e} n_e T_e Q_e$, in addition to possible drive via $T^{\parallel}_{\phi e}$, one would naively expect an enhancement of f_L by at least $\sim Q_e/Q_i$. This does not appear to occur for the runs plotted in Fig. 5, although it is not clear why. Perhaps electron fluctuations are more elongated along the field, thus reducing $c_{\mathcal{K}e}$ due to poloidal variation of $\mathcal{K}$? Perhaps the electron-driven fluctuations occur at smaller perpendicular wavelengths, where drift frequencies are too high to allow for effective ion Landau damping? In any case, the result does not seem to be general, since electrons may at least modestly enhance ion Landau damping in other cases, as we will see in the $\hat{s}$ scan later in this section and in the T_e/T_i scan in Sec. III C.

The three points in Fig. 5 with significantly increased f_L all had stronger density gradients $R/L_n \geq 3$. These points can still be fit with $f_L \approx f_L^{\mathcal{K}i}$, equivalently $c_{\mathcal{K}i} \approx T^{\parallel}_{\phi i}/n_i T_i Q_i$, simply by choosing a larger but still plausible value for $c_{\mathcal{K}i}$, as plotted in Fig. 5.[67] This suggests

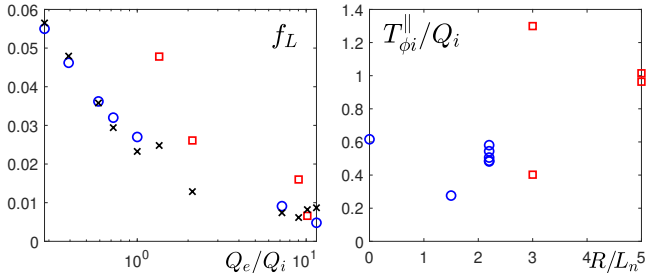

Figure 5. Landau-damping fraction f_L as a function of Q_e/Q_i (left) and $T^{\parallel}_{\phi i}/Q_i$ as a function of R/L_n (right) for the runs from Table I (blue circles for $R/L_n < 3.0$, red squares for $R/L_n \geq 3.0$), along with $f_L^{\mathcal{K}i}$ estimated using $c_{\mathcal{K}i} = 0.5$ (left, black crosses). All of the outliers with f_L significantly above the estimate have $R/L_n \geq 3$.

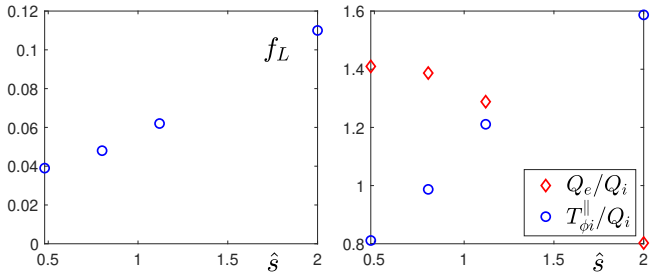

Figure 6. f_L (blue circles, left), $T^{\parallel}_{\phi i}/Q_i$ (blue circles, right), and Q_e/Q_i (red diamonds right) as a function of magnetic shear $\hat{s}$. f_L increases strongly enough with increasing shear $\hat{s}$ that at the largest $\hat{s} = 2.0$, it can no longer be plausibly explained on the basis of $T^{\mathcal{K}}_{\phi i}$ alone ($T^{\parallel}_{\phi i}/Q_i$, equal to the $c_{\mathcal{K}i}$ inferred from assuming $f_L^{\mathcal{K}i} = f_L$, exceeds 4/3).

that steeper R/L_n may simply be allowing a stronger ion Landau damping from Q_i rather than an enhanced role of Q_e.

Although most runs (including all in Table I) had the default shear $\hat{s} = 0.8$, we tried modifications of one run ($R/L_{T_i} = 6.0$, $R/L_{T_e} = 10.5$, $R/L_n = 5.0$), varying $\hat{s}$ to 0.48, 1.12, and 2.0. As shown in Fig. 6, f_L increases strongly with increasing shear. Although some of this can be attributed to decreasing Q_e/Q_i, the $c_{\mathcal{K}i}$ inferred from $f_L \approx f_L^{\mathcal{K}i}$ increases beyond the plausible upper bound[68] of 4/3 at the highest $\hat{s} = 2.0$, suggesting that by this point (at least) electrons must be making a nonnegligible contribution to $U_{\delta E}$, allowing it to drive stronger ion Landau damping.

As plotted in Fig. 7, equation (13) seems to capture the variation of $\Pi_{\varphi i}$ quite well over this scan. Some discrepancy may occur because of contributions of $\Pi^{(1)}_{\varphi i}$, which is not included in the estimate (13), and which only vanishes in the statistical average.

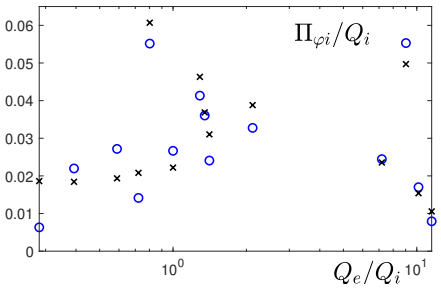

Figure 7. Ion momentum flux $\Pi_{\varphi i}$ (blue circles) and its estimate using (13) (black x's), both normalized to Q_i, including data from Q_e/Q_i and $\hat{s}$ scans.

C. Collisional kinetic electron runs

The inclusion of collisions again alters the free-energy balance [(4) and (5)], with the strongest effect expected from collisional detrapping of electrons. In this section, we simulate (1) and (2) including collisional pitch-angle scattering for the electrons. We do two separate scans: first electron collisionality ν_e (normalized to $R_{\rm ref}/v_{\rm thref}$),[69] then T_e/T_i at fixed, nonzero ν_e.

For the first scan, we fix $R/L_{T_e} = 10.0$ and $R/L_n = 5.0$ and vary ν_e, for both $R/L_{T_i} = 5.0$ and $R/L_{T_i} = 0.1$. As shown in Fig. 8, the normalized heat fluxes (Q_e and Q_i), momentum flux ($\Pi_{\varphi i}$) and particle flux (Γ_i) all decrease with increasing ν_e. This is presumably related to a decrease in the amplitude of the turbulent fluctuations, as exhibited by $(\delta n)_{\rm rms}$, the rms amplitude of normalized density fluctuations at the outboard midplane, and $\phi_{\rm na}$, the rms amplitude of the non-axisymmetric part of the potential ϕ. In addition to collisional weakening of the trapped-electron response, this may also be related to an increase in the relative rms amplitude of axisymmetric potential fluctuations $\phi_{\rm a}$ (predominantly zonal flows), as compared to $\phi_{\rm na}$. Despite these variations, the ion-Landau-damping fraction f_L and the Prandtl number Pr (calculated quasi-linearly at $k_y \approx 0.35$) appear to depend only weakly on collisionality at these fixed gradients.

The toroidal (k_y) spectra of non-axisymmetric potential fluctuations are plotted in Fig. 9. As they show, increasing collisionality not only decreases the overall amplitude of the turbulence, but also shifts the fluctuations to smaller spatial scales.

Although the variation of f_L with ν_e is weak, it continues to be fairly well captured by the ion-curvature estimate $f_L^{\mathcal{K}i}$ with constant $c_{\mathcal{K}i}$ (0.95 for $R/L_{T_i} = 5$, 1.25 for $R/L_{T_i} = 0.1$), as shown in Fig. 10. The plotted ratio $T^{\parallel}_{\phi i}/Q_i$, equal to the $c_{\mathcal{K}i}$ inferred by setting $f_L^{\mathcal{K}i} = f_L$, also varies only weakly with ν_e at fixed R/L_{T_i}. Note that while Q_e/Q_i varies only weakly for $R/L_{T_i} = 5$, remaining close to 2 for all plotted ν_e, it varies more strongly for $R/L_{T_i} = 0.1$, increasing from about 5.5 at $\nu_e \approx 0.0122$ to nearly 11 for $\nu_e \approx 4.9730$.

Since the mean-squared fluctuation amplitude and ion heat flux are closely related, it could be that the ap-

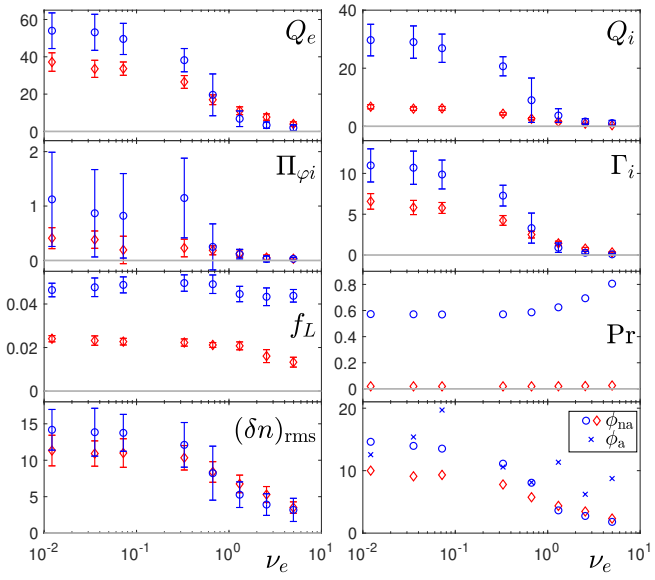

Figure 8. Electron (Q_e) and ion (Q_i) heat flux, momentum flux ($\Pi_{\varphi i}$), particle flux (Γ_i), ion-Landau-damping fraction (f_L), Prandtl number (Pr), rms density fluctuation amplitude at the outboard midplane $(\delta n)_{\rm rms}$, and the rms amplitude of the non-axisymmetric potential ($\phi_{\rm na}$), all as functions of ν_e at fixed $R/L_{T_e} = 10$, $R/L_n = 5$, and for steep ($R/L_{T_i} = 5$, blue circles) and flat ($R/L_{T_i} = 0.1$, red diamonds) ion temperature gradients. Error bars indicate the standard deviation. In the lower-right plot, blue x's indicate the rms amplitude of the axisymmetric potential $\phi_{\rm a}$ for $R/L_{T_i} = 5$.

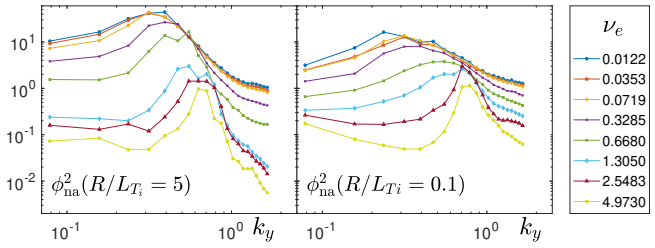

Figure 9. Toroidal (k_y) spectra of non-axisymmetric potential fluctuations for $R/L_{T_i} = 5$ (left) and $R/L_{T_i} = 0.1$ (right). Increasing collisionality reduces the overall amplitude and shifts the fluctuations to higher k_y.

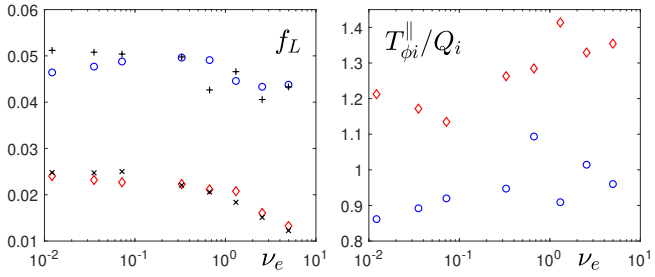

Figure 10. Left: Landau fraction f_L, compared with the estimate $f_L^{\mathcal{K}i}$ (black plus signs and x's), evaluated with constant $c_{\mathcal{K}i}$ of 0.95 for $R/L_{T_i} = 5$ and 1.25 for $R/L_{T_i} = 0.1$. Right: $T^{\parallel}_{\phi i}/Q_i$, equal to the $c_{\mathcal{K}i}$ inferred by setting $f_L^{\mathcal{K}i} = f_L$. Blue circles for $R/L_{T_i} = 5$ and red diamonds for $R/L_{T_i} = 0.1$.

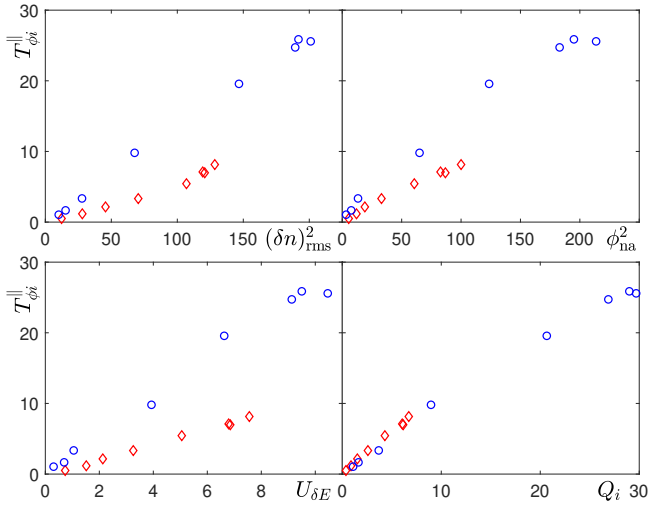

Figure 11. Total energy through ion Landau damping $T^{\parallel}_{\phi i}$ as a function of mean-squared amplitude of outboard-midplane density fluctuations $[(\delta n)^2_{\rm rms}$, upper left] and of the non-axisymmetric part of the potential ($\phi^2_{\rm na}$, upper right), as well as of the estimated $\boldsymbol{E}\times\boldsymbol{B}$ energy $U_{\delta E}$ (lower left) and the ion heat flux Q_i (lower right), for $R/L_{T_i} = 5$ (blue circles) and $R/L_{T_i} = 0.1$ (red diamonds). Although $T^{\parallel}_{\phi i}$ is roughly linear at fixed R/L_{T_i} in all four plots, the two ion temperature gradients only fall on the same line as a function of Q_i.

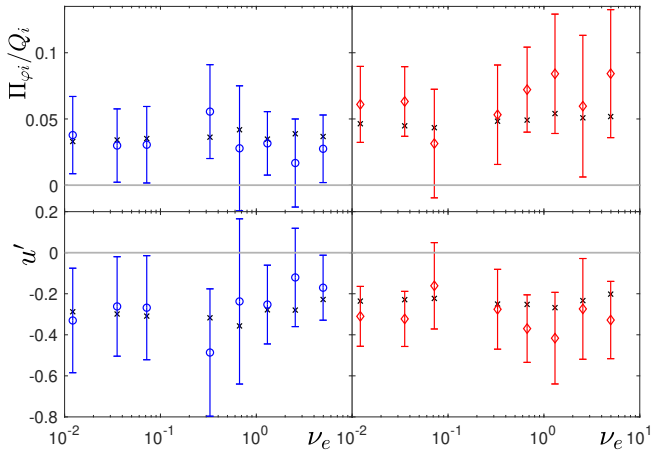

Figure 12. Normalized momentum flux $\Pi_{\varphi i}/Q_i$ (upper) and estimated rotation gradient u' (lower) for $R/L_{T_i} = 5$ (left) and $R/L_{T_i} = 0.1$ (right). Estimates based on f_L are indicated with black x's. The measured values show more variation than the estimates. This may be due to the wide fluctuation of $\Pi_{\varphi i}$ (error bars), due to the leading-order contribution $\Pi^{(1)}_{\varphi i}$, which only vanishes in the statistical average.

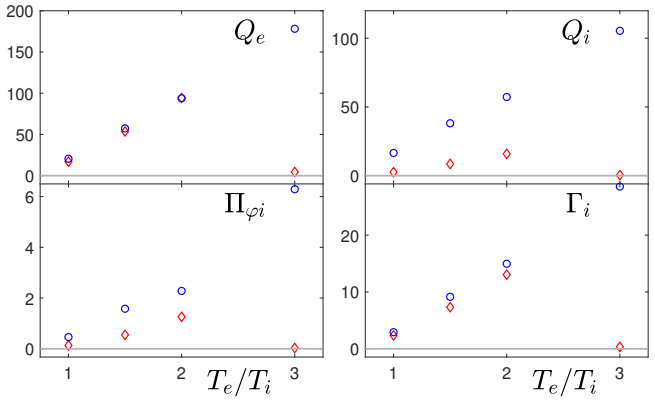

Figure 13. The normalized fluxes Q_e (upper left), Q_i (upper right), $\Pi_{\varphi i}$ (lower left), and Γ_i (lower right) as a function of T_e/T_i, with blue circles for $R/L_{T_i} = 6.0$ and red diamonds for $R/L_{T_i} = 0.1$. Recall that the flux normalizations are species dependent.

parent relation of $T^{\parallel}_{\phi i}$ and Q_i is actually indirect, via a joint dependence on the fluctuation amplitude. However, Fig. 11 shows that while the ion-Landau-damping transfer $T^{\parallel}_{\phi i}$ does in fact depend about linearly on the mean-squared amplitude of outboard-midplane density fluctuations $(\delta n)^2_{\rm rms}$ and of non-axisymmetric potential fluctuations $\phi^2_{\rm na}$, as well as on $U_{\delta E}$,[70] the slope of the line is R/L_{T_i} dependent. In contrast, when both the R/L_{T_i} =0.1 and 5 results for $T^{\parallel}_{\phi i}$ are plotted as a function of Q_i, they collapse onto the same line. This suggests, for these runs at least, that the energy supply for ion Landau damping continues to be primarily limited by $T^{\mathcal{K}}_{\phi i}$, the ion-curvature energy transfer from $U_{\delta i}$ to $U_{\delta E}$.

Finally, Figure 12 shows that the f_L-based estimates from (13) and (16) roughly capture the variation of $\Pi_{\varphi i}/Q_i$ and inferred velocity gradient u' from these collisionality scans. For this comparison, it is important to recall that (13) and (16) only predict the symmetry-breaking $\Pi^{(2)}_{\varphi i}$ portion of the momentum flux, while the measured $\Pi_{\varphi i}$ also retains the leading-order contribution $\Pi^{(1)}_{\varphi i}$, which only vanishes in the statistical average. The effect of this can be seen in the wide error bars for $\Pi_{\varphi i}/Q_i$ and u', derived from the standard deviation of measured $\Pi_{\varphi i}$.

As an alternate cut through parameter space, we conducted a series of runs varying T_e/T_i, with fixed $\nu_e \approx 0.67$, $R/L_{T_e} = 10.5$, $R/L_n = 5$, and for two ion temperature gradients $R/L_{T_i} = 6.0$ and $R/L_{T_i} = 0.1$. Other parameters stayed at default values, including $T_i = 1$. In general, all the fluxes (Q_e, Q_i, $\Pi_{\varphi i}$, and Γ_i) increase with increasing T_e/T_i (Figure 13), except for the single case $T_e/T_i = 3, R/L_{T_i} = 0.1$, for which the turbulence was strongly suppressed. Recalling the species-dependent heat-flux normalizations, the ratio of dimensional heat fluxes is T_eQ_e/T_iQ_i, which is an increasing function of T_e/T_i.

In contrast to our ν_e-scan results, the ion Landau damping in these runs seems to respond quite clearly to electron free-energy supply. As shown in Figure 14, the ratio $T^{\parallel}_{\phi i}/Q_i$ increases with increasing temperature ratio T_e/T_i, exhibiting a roughly linear dependence on the heat flux ratio Q_eT_e/Q_iT_i. (Unfortunately, we do not have a reliable result for $T^{\parallel}_{\phi i}$ or f_L for the quenched case

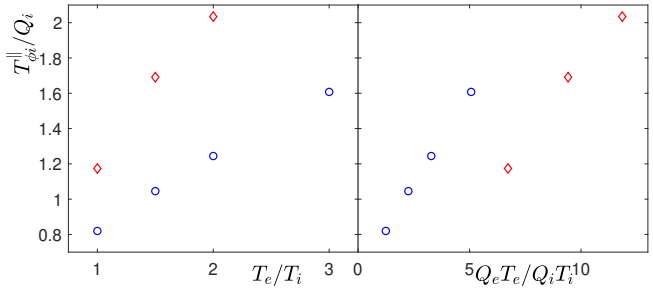

Figure 14. The ratio $T^{\|}_{\phi i}/Q_i$, equal to the $c_{\mathcal{K}i}$ inferred by setting $f_L^{\mathcal{K}i} = f_L$, as a function of T_e/T_i (left) and of the heat flux ratio Q_eT_e/Q_iT_i (right), with red diamonds for $R/L_{T_i} = 0.1$ and blue circles for $R/L_{T_i} = 6$. The ratio has an approximately linear dependence on the electron heat flux, suggesting that electrons are driving some ion Landau damping in this case.

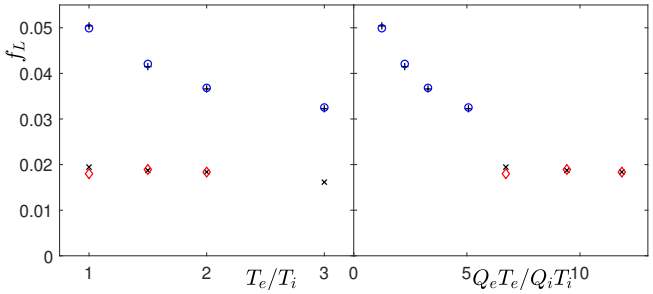

Figure 15. The Landau-damping fraction f_L (red diamonds for $R/L_{T_i} = 0.1$, blue circles for $R/L_{T_i} = 6$) as a function of T_e/T_i (left) and of Q_eT_e/Q_iT_i (right). The estimates for f_L (black x's for $R/L_{T_i} = 0.1$, black +'s for $R/L_{T_i} = 5$) are summed curvature drive $f_L^{\mathcal{K}i} + f_L^{\mathcal{K}e}$, with constant $c_{\mathcal{K}i}$ (0.26 for $R/L_{T_i} = 0.1$, 0.58 for $R/L_{T_i} = 6$) and $c_{\mathcal{K}e}$ (0.15 for $R/L_{T_i} = 0.1$ and 0.20 for $R/L_{T_i} = 6$).

T_e/T_i=3,$R/L_{T_i} = 0.1$.) In order to obtain a reasonable estimate for f_L, we must incorporate electron curvature contributions, taking $f_L \approx f_L^{\mathcal{K}i} + f_L^{\mathcal{K}e}$ for constant $c_{\mathcal{K}i}$ (0.26 for $R/L_{T_i} = 0.1$ and 0.58 for $R/L_{T_i} = 6$) and $c_{\mathcal{K}e}$ (0.15 for $R/L_{T_i} = 0.1$ and 0.20 for $R/L_{T_i} = 6$), see Figure 15.

As before, Equation (13) provides a good estimate for the normalized momentum flux $\Pi_{\varphi i}/Q_i$ in terms of f_L (Figure 16). The normalized momentum flux increases roughly linearly with T_e/T_i and with T_eQ_e/T_iQ_i, except for the quenched case ($R/L_{T_i} = 0.1, T_e/T_i = 3$).

IV. CONCLUSION

Ion Landau damping interacts with a geometrical correction to the ExB drift to cause a non-diffusive outward flux of co-current toroidal angular momentum.[46] Quantitative evaluation of this momentum flux requires nonlinear simulations to determine f_L, the fraction of fluctuation free energy that passes through ion Landau damping (12), in fully developed turbulence. Nonlinear gyrokinetic simulations with the GKW code[48] confirm the presence of the symmetry-breaking momentum flux (Figures 2, 7, 12, 16). For simulations with adiabatic electrons, f_L scales inversely with R/L_{T_i} (Figure 4), because only ion curvature drive $T^{\mathcal{K}}_{\phi i}$ can supply free energy to the electrostatic potential (18). Although kinetic electrons should in principle relax this restriction, the ion Landau damping measured in collisionless kinetic-electron simulations remained restricted to levels comparable with ion curvature drive $T^{\mathcal{K}}_{\phi i}$ (Figure 5), except for a case with strong magnetic shear $\hat{s}$ (Figure 6). A set of simulations scanning collisionality ν_e for electron pitch-angle scattering showed only a weak dependence of f_L on ν_e at fixed gradients (Figure 8). However, collisional-electron simulations with T_e/T_i above unity unambiguously showed electron-curvature drive of ion Landau damping (Figures 14 and 15) and a corresponding enhancement of the symmetry-breaking momentum flux (Figure 16).

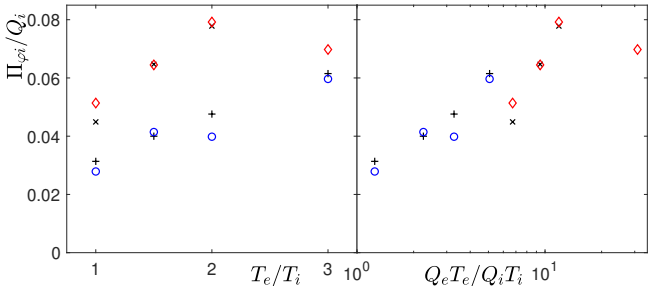

Figure 16. The ratio $\Pi_{\varphi i}/Q_i$ (red diamonds for $R/L_{T_i} = 0.1$, blue circles for $R/L_{T_i} = 5$) versus the estimate from (13) (black x's for $R/L_{T_i} = 0.1$, black +'s for $R/L_{T_i} = 5$), as a function of T_e/T_i (left) and of T_eQ_e/T_iQ_i (right).

ACKNOWLEDGMENTS

Helpful discussions with C. Angioni, E. Fable, G. Hammett, P. Helander, J. Krommes, A. Peeters, and B. Scott, and funding by US Dept. of Energy, Office of Science, Contract DE-AC02-09CH11466 are gratefully acknowledged.

REFERENCES

[1] E. J. Strait, T. S. Taylor, A. D. Turnbull, J. R. Ferron, L. L. Lao, B. Rice, O. Sauter, S. J. Thompson, and D. Wróblewski, Phys. Rev. Lett. **74**, 2483 (1995).
[2] E. J. Doyle, W. A. Houlberg, Y. Kamada, V. Mukhovatov, T. H. Osborne, A. Polevoi, G. Bateman, J. W. Connor, J. G. Cordey, T. Fujita, *et al.*, Nucl. Fusion **47**, S18 (2007).
[3] J. S. deGrassie, Plasma Phys. Control. Fusion **51**, 124047 (2009).
[4] C. Angioni, Y. Camenen, F. J. Casson, E. Fable, R. M. McDermott, A. G. Peeters, and J. E. Rice, Nucl. Fusion **52**, 114003 (2012).
[5] J. E. Rice, Plasma Phys. Control. Fusion **58**, 083001 (2016).

[6] T. Stoltzfus-Dueck, Plasma Phys. Control. Fusion **61**, 124003 (2019).
[7] J. E. Rice, W. D. Lee, E. S. Marmar, P. T. Bonoli, R. S. Granetz, M. J. Greenwald, A. E. Hubbard, I. H. Hutchinson, J. H. Irby, Y. Lin, D. Mossessian, J. A. Snipes, S. M. Wolfe, and S. J. Wukitch, Nucl. Fusion **44**, 379 (2004).
[8] J. S. deGrassie, K. H. Burrell, L. R. Baylor, W. Houlberg, and J. Lohr, Phys. Plasmas **11**, 4323 (2004).
[9] T. Stoltzfus-Dueck, A. N. Karpushov, O. Sauter, B. P. Duval, B. Labit, H. Reimerdes, W. A. J. Vijvers, Y. Camenen, and the TCV Team, Phys. Rev. Lett. **114**, 245001 (2015).
[10] A. Bortolon, B. P. Duval, A. Pochelon, and A. Scarabosio, Phys. Rev. Lett. **97**, 235003 (2006).
[11] J. S. deGrassie, J. E. Rice, K. H. Burrell, R. J. Groebner, and W. M. Solomon, Phys. Plasmas **14**, 056115 (2007).
[12] J. E. Rice, C. Gao, M. L. Reinke, P. H. Diamond, N. T. Howard, H. J. Sun, I. Cziegler, A. E. Hubbard, Y. A. Podpaly, W. L. Rowan, *et al.*, Nucl. Fusion **53**, 033004 (2013).
[13] Y. Camenen *et al.*, Plasma Phys. Control. Fusion **59**, 034001 (2017).
[14] D. H. Na *et al.*, Nucl. Fusion **57**, 126008 (2017).
[15] A. E. White *et al.*, Phys. Plasmas **20**, 056106 (2013).
[16] J. W. Yoo, S. G. Lee, S. H. Ko, J. Seol, H. H. Lee, and J. H. Kim, Phys. Plasmas **24**, 072510 (2017).
[17] M. F. F. Nave *et al.*, Nucl. Fusion **57**, 034002 (2017).
[18] Y. J. Shi *et al.*, Nucl. Fusion **57**, 066040 (2017).
[19] C. Angioni, R. M. McDermott, F. J. Casson, E. Fable, A. Bottino, R. Dux, R. Fischer, Y. Podoba, T. Pütterich, F. Ryter, E. Viezzer, and ASDEX Upgrade Team, Phys. Rev. Lett. **107**, 215003 (2011).
[20] R. M. McDermott, C. Angioni, G. D. Conway, R. Dux, E. Fable, R. Fischer, T. Pütterich, F. Ryter, E. Viezzer, and the ASDEX Upgrade Team, Nucl. Fusion **54**, 043009 (2014).
[21] J. E. Rice, M. J. Greenwald, Y. A. Podpaly, M. L. Reinke, P. H. Diamond, J. W. Hughes, N. T. Howard, Y. Ma, I. Cziegler, B. P. Duval, *et al.*, Phys. Plasmas **19**, 056106 (2012).
[22] A. G. Peeters, C. Angioni, A. Bortolon, Y. Camenen, F. J. Casson, B. Duval, L. Fiederspiel, W. A. Hornsby, Y. Idomura, T. Hein, *et al.*, Nucl. Fusion **51**, 094027 (2011).
[23] P. H. Diamond, C. J. McDevitt, Ö. D. Gürcan, T. S. Hahm, W. X. Wang, E. S. Yoon, I. Holod, Z. Lin, V. Naulin, and R. Singh, Nucl. Fusion **49**, 045002 (2009).
[24] B. Scott and J. Smirnov, Phys. Plasmas **17**, 112302 (2010).
[25] A. J. Brizard and N. Tronko, Phys. Plasmas **18**, 082307 (2011).
[26] S. D. Scott, P. H. Diamond, R. J. Fonck, R. J. Goldston, R. B. Howell, K. P. Jaehnig, G. Schilling, E. J. Synakowski, M. C. Zarnstorff, C. E. Bush, *et al.*, Phys. Rev. Lett. **64**, 531 (1990).
[27] W. D. Lee, J. E. Rice, E. S. Marmar, M. J. Greenwald, I. H. Hutchinson, and J. A. Snipes, Phys. Rev. Lett. **91**, 205003 (2003).
[28] S. M. Kaye, W. Solomon, R. E. Bell, B. P. LeBlanc, F. Levinton, J. Menard, G. Rewoldt, S. Sabbagh, W. Wang, and H. Yuh, Nucl. Fusion **49**, 045010 (2009).
[29] Y. Sarazin *et al.*, Nucl. Fusion **51**, 103023 (2011).
[30] S. Jolliet and Y. Idomura, Nucl. Fusion **52**, 023026 (2012).
[31] S. Ku *et al.*, Nucl. Fusion **52**, 063013 (2012).
[32] Y. Idomura, Phys. Plasmas **21**, 022517 (2014).
[33] R. E. Waltz, G. M. Staebler, and W. M. Solomon, Phys. Plasmas **18**, 042504 (2011).
[34] W. X. Wang, B. A. Grierson, S. Ethier, J. Chen, E. Startsev, and P. H. Diamond, Phys. Plasmas **24**, 092501 (2017).
[35] W. A. Hornsby, C. Angioni, Z. X. Lu, E. Fable, I. Erofeev, R. McDermott, A. Medvedeva, A. Lebschy, A. G. Peeters, and the ASDEX Upgrade Team, Nucl. Fusion **58**, 056008 (2018).
[36] R. E. Waltz, G. M. Staebler, J. Candy, and F. L. Hinton, Phys. Plasmas **14**, 122507 (2007).
[37] F. J. Casson, A. G. Peeters, Y. Camenen, W. A. Hornsby, A. P. Snodin, D. Strintzi, and G. Szepesi, Phys. Plasmas **16**, 092303 (2009).
[38] T. Sung, R. Buchholz, F. J. Casson, E. Fable, S. R. Grosshauser, W. A. Hornsby, P. Migliano, and A. G. Peeters, Phys. Plasmas **20**, 042506 (2013).
[39] W. A. Hornsby, C. Angioni, E. Fable, P. Manas, R. McDermott, A. G. Peeters, M. Barnes, F. Parra, and the ASDEX Upgrade Team, Nucl. Fusion **57**, 046008 (2017).
[40] H. Sugama, T. H. Watanabe, M. Nunami, and S. Nishimura, Plasma Phys. Control. Fusion **53**, 024004 (2011).
[41] F. I. Parra, M. Barnes, and A. G. Peeters, Phys. Plasmas **18**, 062501 (2011).
[42] A. G. Peeters and C. Angioni, Phys. Plasmas **12**, 072515 (2005).
[43] R. R. Dominguez and G. M. Staebler, Phys. Fluids B **5**, 3876 (1993).
[44] Y. Camenen, A. G. Peeters, C. Angioni, F. J. Casson, W. A. Hornsby, A. P. Snodin, and D. Strintzi, Phys. Rev. Lett. **102**, 125001 (2009).
[45] T. Stoltzfus-Dueck, Phys. Plasmas **24**, 030702 (2017).
[46] T. Stoltzfus-Dueck and B. Scott, Nucl. Fusion **57**, 086036 (2017).
[47] L. Landau, J. Phys. (U.S.S.R.) **10**, 25 (1946).
[48] A. G. Peeters, Y. Camenen, F. J. Casson, W. A. Hornsby, A. P. Snodin, D. Strintzi, and G. Szepesi, Comput. Phys. Commun. **180**, 2650 (2009).

[49] This can be obtained by simply setting $A_\parallel$ to zero and ψ_e to ϕ.

[50] PCC's (84) has a typo. The rightmost form should have a factor of $(T^k_{\rm ref})^{-2}$ rather than $(T^k_{\rm ref})^{-1}$.

[51] This implies that the normalized quantities satisfy $m_s v_{ts}^2 = T_s$.

[52] We equate $B_{\rm ref}$ with SDS's B_0.

[53] Since SDS used cgs units, this must be defined slightly differently than PCC, which used SI units.

[54] This remains roughly equivalent to PCC's slightly different treatment, which normalizes all gradients using $R_{\rm ref}$, but then uses a Fourier representation in the perpendicular directions and rescales the wavenumbers by ρ_*.

[55] We normalize our parallel coordinate s such that it is a unit-periodic poloidal Hamada angle, like PCC. We normalize the parallel gradient operator $\nabla_\parallel$ to $R^{-1}_{\rm ref}$, but perpendicular gradients to $\rho^{-1}_{\rm ref}$. For consistency, we must normalize our curvature operator $\mathcal{K}$ to $(2c/B_{\rm ref}R_{\rm ref}\rho_{\rm ref})$ and $\int \mathrm{d}\mathcal{W}$ to $(v_{ts}^{\rm dim})^3$. We normalize F'_{sM} to $[n_s^{\rm dim}/(v_{ts}^{\rm dim})^3 R_{\rm ref}]$.

[56] In the dimensional variables of SDS, we define $\partial_r \doteq V'\partial_V$. In the notation of PCC, we define $\partial_r \doteq R^{-1}_{\rm ref}\partial_\psi$. For consistency, we will set $V' = R^{-1}_{\rm ref}\partial_\psi V$ throughout this article. Note also that PCC's u' has a different sign convention than ours: they take Ω and u' to be positive for toroidal rotation in the direction of the toroidal magnetic field. However, since the toroidal magnetic field is in the $+\hat{\varphi}$ direction for all runs in this article, that distinction does not matter here.

[57] PCC's (66) and (67) are each missing a factor of R in the u' term, a typo.

[58] The finite difference treatment of s and $v_\parallel$ derivatives is non-conservative, and includes explicit hyperviscous dissipation when the derivatives act on f_s. Magnetic shear introduces some parallel connections to unresolved k_x at the s boundaries, which are treated with (lossy) outgoing boundary conditions. The Poisson bracket is treated with a lossy dealiased pseudo-spectral method, adding dissipation at large k_x and k_y. See PCC for details.

[59] In the notation of PCC, $b_p \doteq (4\pi\mathcal{E}^{\psi\zeta})^{-1}$, with $\mathcal{E}^{\psi\zeta} \to q\sqrt{1-\epsilon^2}/4\pi\epsilon$ in this article, where we always use circular geometry with positive toroidal magnetic field ($s_{\rm B} = +1$). In the dimensional notation of SDS, $b_p \doteq B^\theta V'/2\pi R_{\rm ref} B_0$.

[60] See SDS App. C for the explicit demonstration that ion Landau damping corresponds to energy transfer via $T^\parallel_{\phi i}$.

[61] Recall that R is normalized to $R_{\rm ref}$ and that b_T is the toroidal component of the magnetic direction (unit vector). However, if $T^\parallel_{\phi i}$ and $\Pi^{(2)}_\varphi$ are concentrated at the outboard midplane, this may be a quantitative underestimate, since at the outboard $R^2 \sim (1+\epsilon)^2$.

[62]Viscosity runs are done with only parallel velocity shear, that is, the $\boldsymbol{E} \times \boldsymbol{B}$ shear in viscous runs is zero.

[63]In GKW notation, this corresponds to $k_\theta \rho_{\mathrm{ref}} = 0.42$. For all runs in this article, $k_\theta \rho_{\mathrm{ref}} \approx 0.855 k_y$.

[64]In GKW, time is normalized to $R_{\mathrm{ref}}/v_{\mathrm{thref}}$.

[65]The exact value of the average depends on the time window that you select, but it is much smaller than the rms value for any reasonable choice.

[66]A small collisionality is added for numerical purposes.

[67]Recall that $n_i = T_i = 1$ in all of our simulations.

[68]See discussion by (20).

[69]In PCC's notation, assuming deuterium ions, our ν_e is written as $\nu_e \doteq v_{te}\Gamma^{e/i} = 3.95 \cdot 10^{-3} \frac{R_{\mathrm{ref}}(\mathrm{m}) n_{\mathrm{ref}}(10^{19}\mathrm{m}^{-3})}{[T_{\mathrm{ref}}(\mathrm{keV})]^2} \frac{n_i Z^2 \ln \Lambda^{e/i}}{T_e^{3/2}}$.

[70]To evaluate $U_{\delta E}$ for Figure 11, we used the spectral data from Figure 9. We neglected the radial variation (k_x) for the evaluation of the Bessel functions Γ_{0s}.